

Article

NH₂-MIL-125-Derived N-Doped TiO₂@C Visible Light Catalyst for Wastewater Treatment

Wenbin Wang ^{1,2,†}, Wei Qiang ^{1,†}, Chuntao Chen ¹ and Dongping Sun ^{1,*} 

¹ Institute of Chemicobiology and Functional Materials, School of Chemistry and Chemical Engineering, Nanjing University of Science and Technology, Nanjing 210094, China; 18302596016@163.com (W.W.); zhnlq@sina.cn (W.Q.); chchunt@njust.edu.cn (C.C.)

² Guizhou Panjiang Civil Explosion Co., Ltd., Guiyang 551404, China

* Correspondence: hysdp@njust.edu.cn

† These authors contributed equally to this work.

Abstract: The utilization of titanium dioxide (TiO₂) as a photocatalyst for the treatment of wastewater has attracted significant attention in the environmental field. Herein, we prepared an NH₂-MIL-125-derived N-doped TiO₂@C Visible Light Catalyst through an in situ calcination method. The nitrogen element in the organic connector was released through calcination, simultaneously doping into the sample, thereby enhancing its spectral response to cover the visible region. The as-prepared N-doped TiO₂@C catalyst exhibited a preserved cage structure even after calcination, thereby alleviating the optical shielding effect and further augmenting its photocatalytic performance by increasing the reaction sites between the catalyst and pollutants. The calcination time of the N-doped TiO₂@C-450 °C catalyst was optimized to achieve a balance between the TiO₂ content and nitrogen doping level, ensuring efficient degradation rates for basic fuchsin (99.7%), Rhodamine B (89.9%) and tetracycline hydrochloride (93%) within 90 min. Thus, this study presents a feasible strategy for the efficient degradation of pollutants under visible light.

Keywords: titanium dioxide; NH₂-MIL-125; N-doped TiO₂@C; visible light photocatalysis; wastewater pollutants



Citation: Wang, W.; Qiang, W.; Chen, C.; Sun, D. NH₂-MIL-125-Derived N-Doped TiO₂@C Visible Light Catalyst for Wastewater Treatment. *Polymers* **2024**, *16*, 186. <https://doi.org/10.3390/polym16020186>

Academic Editors: Seyed Borhan Mousavi and Grigorios L. Kyriakopoulos

Received: 3 December 2023

Revised: 5 January 2024

Accepted: 5 January 2024

Published: 8 January 2024



Copyright: © 2024 by the authors. Licensee MDPI, Basel, Switzerland. This article is an open access article distributed under the terms and conditions of the Creative Commons Attribution (CC BY) license (<https://creativecommons.org/licenses/by/4.0/>).

1. Introduction

The 21st century is all about global economic development, but there are some problems that we cannot ignore. One of the common concerns is how to maintain or even improve the quality of water. According to the reports of the United Nations Educational, Scientific and Cultural Organization in the World 2021 Water Resources Development Report, as our society continues to grow, we use more and more fresh water in industry, agriculture and urban life. Since 1980, its usage has been increasing by approximately 1% every year, which exacerbates the issue of water pollution [1]. Around 80% of wastewater is being discharged into the environment without any treatment. This leads to water pollution that causes approximately 2 million deaths worldwide annually and leaves many others suffering from chronic diseases [2]. Therefore, we must consider how we can upgrade our existing methods of treating water to meet the growing demand for wastewater disposal.

The composition of wastewater usually includes organic dye pollution and antibiotic pollution, which are typical troublemakers [3]. Organic dye pollution is mainly caused by industries such as textiles, cosmetics, food and paper. It has a strong color, high toxicity to living things, exhibits excellent resistance to oxidation and is tough to break down naturally. All these factors make it a big threat to our ecosystem [4,5]. Basic fuchsin and Rhodamine B are representative organic dyes. The molecular formula of basic fuchsin is C₂₀H₂₀ClN₃. Long-term exposure to basic fuchsin can cause skin cells to become cancerous because its carcinogenic triphenylmethane structure makes it a cationic dye, which is more toxic than anionic dyes. Rhodamine B, with a molecular formula of C₂₈H₃₁ClN₂O₃, is an alkaline

industrial dye that poses direct harm to human health. It belongs to the third class of carcinogens in the list published by the International Agency for Research on Cancer of the World Health Organization (WHO). Antibiotic contamination usually originates from livestock and pharmaceutical industries [6]. It is difficult for animals and humans to fully absorb or transform tetracycline hydrochloride, resulting in over 50% of it being excreted through feces and urine into the environment. As a result, tetracycline hydrochloride can be detected in surface water, groundwater, sediment, soil and even drinking water. This is the main reason for the increase in bacterial resistance among humans. Growing drug resistance leads to higher healthcare costs and makes diseases more challenging to treat. Therefore, the degradation of basic fuchsin, Rhodamine B and tetracycline hydrochloride was studied in this paper's experiments.

Currently, various technologies are being widely studied to address the challenge of water pollution, including biological methods, adsorption methods, membrane separation and photocatalysis. The biological method decomposes pollutants through the adsorption capacity and metabolic processes of bacteria, fungi, yeast, actinomycetes, algae and other microorganisms. This degradation process is simple and stable but requires strict environmental conditions. If researchers operate improperly or without cautionary measures in place, it can easily lead to secondary pollution; therefore, implementing this method on a large scale is not practical [7]. The adsorption method involves the use of physicochemical interactions between the adsorbent material and the pollutant, resulting in the adsorption of pollutants onto the material. Hani et al. reported the processing of MOFs via the three-dimensional (3D) printing of cellulose MOFs as adsorbents and catalysts for water treatment, and the materials offered the complete (>99%) removal of organic dyes within 10 min toward anionic dyes, e.g., methyl blue (MeB). The reaction conditions are mild and fast, and the adsorbent materials can be reused. However, changes in reaction conditions make it easier for them to be released again [8]. Membrane separation is a novel technology that utilizes selective permeation of membranes to separate pollutants from wastewater, including reverse osmosis, microfiltration, ultrafiltration, nanofiltration and other specific methods. It offers simple and pollution-free operation. However, when the membrane becomes blocked by pollutants, restoring it to its original state using existing cleaning technologies can be challenging. As a result, the treatment efficiency of the membrane continuously decreases, and reusing it becomes difficult. In practical applications, membrane separation is often combined with other techniques to enhance utilization [9]. Therefore, photocatalysis, which uses solar excitation to produce strong oxidizing substances, is an effective and promising means for purifying phenolic water. The photocatalytic performance of TiO_2 is affected by the large band gap (3.2 eV of anatase), which can only absorb ultraviolet light, accounting for about 5% of the solar spectrum [10–12]. In addition, the rapid recombination of photogenerated electron–hole pairs in the catalytic process also reduces the photoutilization rate of TiO_2 , resulting in a decrease in the degradation efficiency of organic pollutants [7].

Anatase TiO_2 belongs to the tetragonal system. The octahedral unit TiO_6^{2-} has four edges. The band gap of anatase TiO_2 is 3.2 eV, which is higher than that of rutile TiO_2 (3.0 eV). Although this means that anatase TiO_2 has a narrower range of light absorption, the difference in the conduction band and valence band positions gives the electron–hole pair of anatase TiO_2 a greater positive or negative potential, thus possessing a stronger oxidation capacity. After performing theoretical calculations, Georg et al. [13] demonstrated that the surface of anatase TiO_2 demonstrates a high adsorption capacity for H_2O , O_2 and OH^- , leading to the increased production of active free radicals during catalytic reactions and enhanced photocatalytic activity. During the crystallization process, anatase TiO_2 tends to form small-sized particles with a large specific surface area [14], which is also beneficial for the photocatalytic reaction [15].

Metal–organic frameworks (MOFs) are materials that consist of a self-assembled metal–organic skeleton formed by clusters of metal ions and organic ligands [16]. NH_2 -MIL-125 is a type of MOF that has a large specific surface area and pore volume, and it can facilitate

transmission and diffusion and expose as many active sites as possible [17]. The porous structure of NH₂-MIL-125 allows for a shorter distance for charge carrier transfer, effectively separating photogenerated electron pairs [18]. Furthermore, the large, interconnected 3D open cavities in NH₂-MIL-125 facilitate easy penetration of light, effectively reducing light shielding [19]. The catalyst prepared using NH₂-MIL-125 as the template combines TiO₂ with a carbon matrix, which not only maintains the morphological advantage of the MOF but also limits the aggregation of TiO₂ nanocrystals and improves the electrical conductivity of the TiO₂@C composite [20–24].

In this work, NH₂-MIL-125 was used as a template to synthesize N-doped TiO₂@C composite catalyst with high photocatalytic efficiency via calcination. TiO₂ grew in situ with titanium elements in NH₂-MIL-125 as the core, and the carbon skeleton of NH₂-MIL-125 as a template still existed after calcination. The structure of N/TiO₂@C catalytic materials was characterized using XRD, SEM, TEM, XPS and other testing methods. The natural and photocatalytic properties of N-doped TiO₂@C composites were evaluated.

2. Materials and Methods

2.1. Materials

2-amino-terephthalic acid (99%) was bought from Beijing Bailingwei Technology Co., Ltd., Beijing, China. Dimethylformamide (99.9%) was bought from Aladdin Chemical Co., Ltd., Shanghai, China. Methanol (99.9%) was bought from Jinan Century Tongda Co., Ltd., Jinan, China. Isopropyl titanate (95%) was obtained from Syntechem Co., Ltd., Guangzhou, China.

2.2. Preparation of NH₂-MIL-125

NH₂-MIL-125 was prepared through a hydrothermal reaction. An amount of 1 g of 2-amino-terephthalic acid was added to a mixture of 18 mL of dimethylformamide and 2 mL of methanol. The mixture was stirred and subjected to ultrasonication for 5 min, followed by the addition of 1.2 mL of isopropyl titanate. After stirring and ultrasonication for 5 min, it was transferred to a Teflon autoclave with a volume capacity of 50 mL for heat treatment at 150 °C for 15 h. The resulting yellow powder was collected, centrifuged, washed three times each with dimethylformamide/ethanol and subsequently dried under vacuum conditions at 50 °C for 20 h.

2.3. Preparation of N-Doped TiO₂@C Nanomaterials

N-doped TiO₂@C was prepared via the one-step pyrolysis method. A porcelain boat containing 500 mg of NH₂-MIL-125 powder was positioned at the center of a high-temperature tubular furnace for air-based heat treatment. The tubular furnace operated with a heating rate set to 2 °C·min⁻¹ within a target temperature range spanning from 200 °C to 550 °C while maintaining the desired temperature for two hours. Following the completion of the reaction, we retrieved the resulting powder.

2.4. Characterization

Chemical groups within samples were investigated using a Nicolet IS 20 FTIR spectrometer (Thermo Fisher, Waltham, MA, USA) in the range of 4000–500 cm⁻¹. The X-ray diffraction (XRD) of samples was conducted with an X-ray diffractometer (D8 Advance Bruker, Berlin, Germany). The morphological structure of the cryogels was observed with a JSM-IT500HR scanning electron microscope (SEM) and a transmission electron microscope (TEM) (JEM-2100, JEOL, Kyoto, Japan). The Brunauer–Emmett–Teller (BET) surface area and pore size were tested via nitrogen adsorption and desorption at 77 K with an ASAP automated micromeritics system. The elemental composition of samples was measured via X-ray photoelectron spectroscopy (PHI QUANTERA II, Ulvac-Phi, Kanagawa, Japan). Thermogravimetric analysis (TGA, METTLER TOLEDO TGA/SDTA851) was carried out at a constant heating rate of 10 °C min⁻¹ from 50 °C to 700 °C under a nitrogen atmosphere. The optical performance of the samples was conducted on a UV-3600 spectrophotome-

ter (Shimadzu, Kyoto, Japan). The electrochemical tests, including the electrochemical impedance (EIS), transient photocurrent and Mott–Schottky (M–S), were pictured with an electrochemical workstation (RST5200F, Restile, Gujarat, India). The response of hydroxyl radicals was tested with an electron paramagnetic resonance (EPR) spectrometer (EMXPLUS, Bruker). The contents of C, N and H in the resultant cellulose samples were determined with a Eurovector EA 3000 elemental analyzer in CHN mode.

2.5. Photocatalytic Performance Measurements

Visible light irradiation (more than 400 nm) degraded the basic fuchsin, Rhodamine B and tetracycline hydrochloride, and the photocatalytic properties of various catalysts were studied. All photocatalytic experiments were repeated three times. A 300 W xenon lamp with a filter was used to simulate AM 1.5 G lighting (100 mW/cm^2) as a light source. The circulating water flow in the reactor ensures that the photocatalytic reaction takes place at room temperature. During the degradation process, 20 mg of each photocatalyst was separately dispersed into 30 mL of basic fuchsin, Rhodamine B and tetracycline hydrochloride at a concentration of 15 mg/L. The mixture was subsequently stirred in darkness for 60 min to achieve adsorption–desorption equilibrium. During irradiation, the samples were regularly extracted and filtered using a $0.45 \mu\text{m}$ PTFE needle filter. The resulting solution was measured for absorbance at wavelengths of 546 nm, 554 nm and 370 nm utilizing an ultraviolet–visible spectrophotometer. After degradation, the catalyst underwent recovery through filtration before being washed with deionized water and ethanol. Subsequently, it was dried under vacuum conditions at a temperature of $60 \text{ }^\circ\text{C}$ for twenty hours. Finally, the treated catalyst could undergo multiple tests to evaluate its stability.

3. Results

3.1. Synthesis and Characterization of N-Doped $\text{TiO}_2@\text{C}$

The overall fabrication of the N-doped $\text{TiO}_2@\text{C}$ composite is schematically illustrated in Figure 1a. In order to explore the crystal structure of the sample prepared in the experiment, X-ray diffraction (XRD) tests were first conducted. $\text{NH}_2\text{-MIL-125}$ samples show typical diffraction peaks at 6.67° , 9.62° , 11.48° , 14.90° , 16.50° , 17.89° and 19.42° . The outcomes indicated that the synthesis of $\text{NH}_2\text{-MIL-125}$ was successful and that the produced MOF exhibited acceptable crystallinity. N-doped $\text{TiO}_2@\text{C-450 }^\circ\text{C}$ was obtained via the calcination of $\text{NH}_2\text{-MIL-125}$, and the characteristic peak of $\text{NH}_2\text{-MIL-125}$ totally vanished during the process. The XRD pattern of N-doped $\text{TiO}_2@\text{C-450 }^\circ\text{C}$ was compared with the standard diffraction card of anatase TiO_2 (JCPDSNo.21–1272). It was found that peaks of 25.06° , 38.10° , 47.89° , 53.70° and 61.46° corresponded to the (101), (004), (200), (105) and (204) planes of anatase, respectively. The results show that the pyrolysis of $\text{NH}_2\text{-MIL-125}$ to produce anatase TiO_2 was successful. In addition, the XRD characterization of N-doped $\text{TiO}_2@\text{C}$ was significantly different from different calcination temperatures (Figure 1b,c). The calcination temperature of N-doped $\text{TiO}_2@\text{C-250 }^\circ\text{C}$ was too low, which caused insufficient pyrolysis. The characteristic peaks of $\text{NH}_2\text{-MIL-125}$ can still be seen at 6.63° , 9.65° and 11.64° , but the peak intensity was reduced significantly. This may have been due to the partial disintegration and recombination of the $\text{NH}_2\text{-MIL-125}$ structure. When the temperature of the calcination reached $350 \text{ }^\circ\text{C}$, only a carbon sheath peaked at 13.19° , and no TiO_2 -related peak pattern was visible, indicating that the $\text{NH}_2\text{-MIL-125}$ structure was totally broken down. TiO_2 had not yet formed crystals, and the carbon element that was liberated during the calcination was doped into the compound. The distinctive peak of anatase TiO_2 was clearly seen when the temperature hit $450 \text{ }^\circ\text{C}$. Following that, the intensity of the anatase TiO_2 characteristic peak no longer varied considerably with the rise in calcination temperature, but the crystallinity of TiO_2 was more excellent.

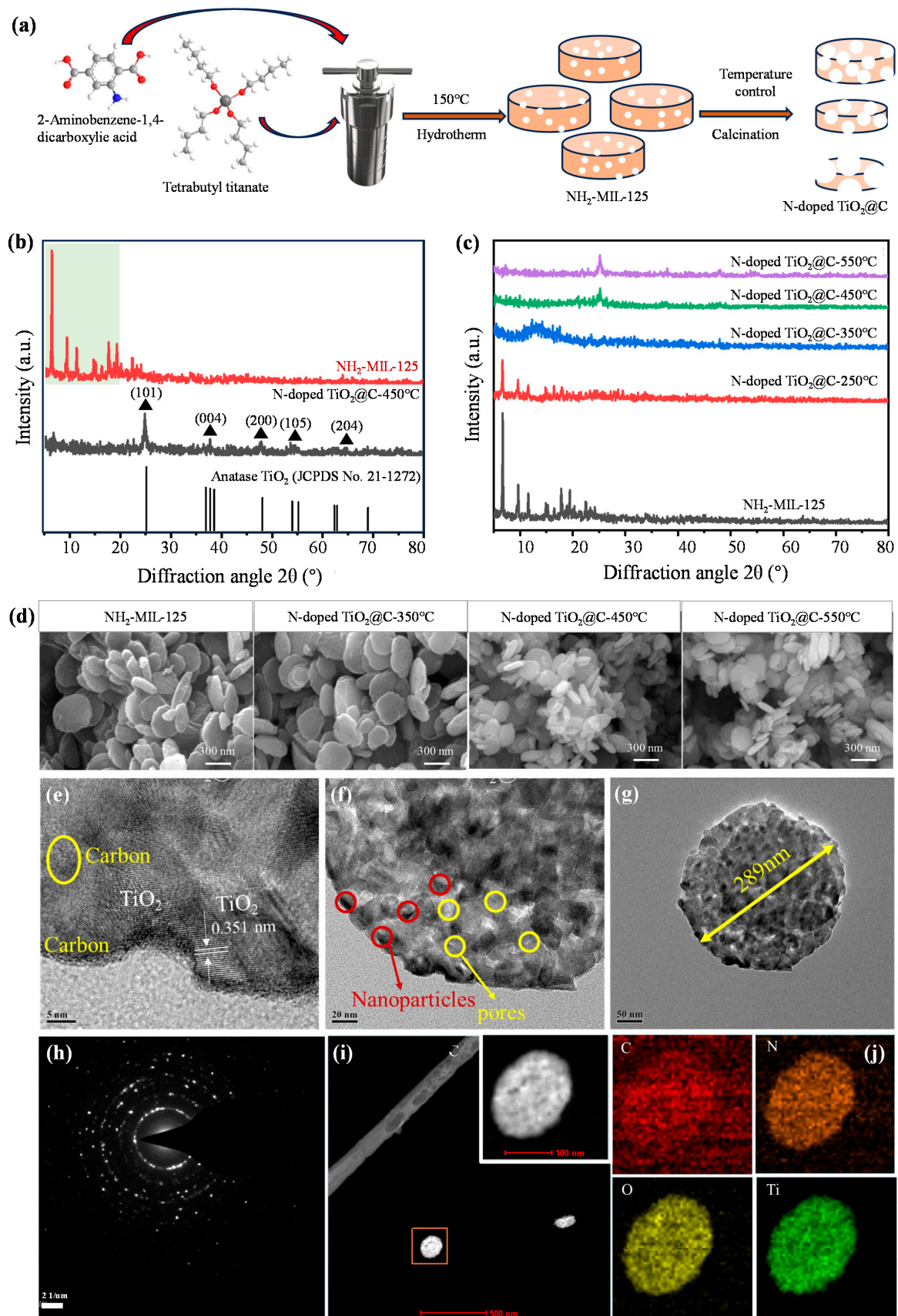


Figure 1. Schematic diagram and characterization of N-doped TiO₂@C composite. **(a)** Fabrication of N-doped TiO₂@C composite. **(b,c)** NH₂-MIL-125 and N-doped TiO₂@C composites with calcination

temperatures of 250 °C, 350 °C, 450 °C and 550 °C. (d) SEM images of NH₂-MIL-125 and N-doped TiO₂@C composites with calcination temperatures of 250 °C, 350 °C, 450 °C and 550 °C. (e–g) TEM images of N-doped TiO₂@C-450 °C. (h) Electron diffraction image of N-doped TiO₂@C-450 °C. (i,j) Element mapping of N-doped TiO₂@C-450 °C.

From the SEM images, the prepared NH₂-MIL-125 showed a circular flake shape with an average diameter of about 422 nm (Figure 1d). In N-doped TiO₂@C-450 °C, the thickness of TiO₂-like circular tablets was about 50 nm, and the diameter was about 140 nm. The sample had a thickness of around 60 nm and a diameter of about 370 nm for N-doped TiO₂@C-350 °C. And for the N-doped TiO₂@C-250 °C sample, its thickness was around 70 nm, and its diameter was about 450 nm. It is evident that, as the calcination temperature rose, the average particle size of the sample particles shrank to some extent while maintaining its round pill shape. This might have been because, as the calcination temperature rose, the network structure of NH₂-MIL-125 gradually lost its capacity to crystallize, and the organic molecules in the skeleton broke down.

The shape and crystal structure of N-doped TiO₂@C-450 °C composites were obtained via TEM. The observation of amorphous carbon shows that a large amount of TiO₂ was distributed in the carbon matrix and finally formed the TiO₂@C composite. The sample obtained after calcination still maintained a porous structure, as seen by the presence of TiO₂ nanoparticles and pores (Figure 1e,f). This porous construction can increase photocatalytic efficiency by exposing as many active sites as feasible while also facilitating the transmission and diffusion of electrons during catalysis. In the adsorption experiment, more investigation into the porous structure was conducted on N/TiO₂@C-450 °C, on which a lattice spacing of 0.351 nm was found, compatible with the lattice spacing of the crystal planes of anatase TiO₂ (101) (Figure 1g). From TEM observations, the diameter of the N-doped TiO₂@C-450 °C was approximately 289 nm (Figure 1g). On N-doped TiO₂@C-450 °C, a lattice spacing of 0.351 nm was found, which was compatible with the lattice spacing of the crystal planes of anatase TiO₂ (101) (Figure 1h). Titanium, oxygen, carbon and nitrogen were all further confirmed by the element mapping (Figure 1i,j). It is evident that, on N-doped TiO₂@C-450 °C, the distribution of titanium, oxygen, carbon and nitrogen was quite uniform. It can be argued that, during calcination, the nitrogen element contained in the organic ligand 2-amino-terephtharic acid was released and then doped into the sample. The titanium element in NH₂-MIL-125 was grown in situ to form TiO₂, which was uniformly dispersed in the porous carbon skeleton, and ultimately, the nitrogen-doped TiO₂@C was successfully formed.

The elemental composition and valence information of N-doped TiO₂@C were subsequently examined using X-ray photoelectron spectroscopy (XPS), which was utilized to test the material composition (Figure 2a,b). When the temperature was too high, all nitrogen was released and was no longer doped into the TiO₂@C composite, and the peak value of carbon and nitrogen decreased with the increase in calcination temperature. When the temperature reached 550 °C, the peak of nitrogen was close to zero. However, the proper calcination temperature was crucial, as the XRD pattern analysis showed that anatase TiO₂ was difficult to produce or had poor crystallinity at too low temperatures. A calcination temperature of 450 °C could be used as the equilibrium temperature between nitrogen doping and TiO₂ crystallinity. Three peaks at 532.0 eV, 530.9 eV and 528.9 eV, which are associated with the C–O bond, C=O bond and Ti–O bond, respectively, can be seen in the XPS spectra of O 1s (Figure 2c). The surface hydroxyl oxygen, which is essential for the photodegradation of contaminants, was responsible for the development of the C–O bond. To fight contaminants, the hydroxyl radical OH• could be created when it interacted with photogenic holes. N 1s (Figure 2d) displayed a broad peak between 398.4 and 399.4 eV. It is consistent with other results and typical Ti–N structures in nitrogen-doped TiO₂ [25]. The C=C peaks (Figure 2e) at 288.2 eV, 286.4 eV, 285.6 eV and 284.2 eV correspond to C=O, C–O, C–N and C=C, respectively. For pure anatase TiO₂, Ti–O peaks were located at 458.5 eV and

464.5 eV. The Ti 2p peaks for N-doped TiO₂@C-450 °C were 457.5 eV and 463.5 eV, which is a 6.0 eV energy split. The peaks of Ti 2p shown in Figure 2f centered at about 463.2 eV and 457.5 eV belonged to Ti 2p_{3/2} and Ti 2p_{1/2}, respectively, which confirm the Ti⁴⁺ species in the form of TiO₂ nanoparticles. The Ti 2p peak for N-doped TiO₂@C-450 °C was slightly shifted toward a lower binding energy when compared to pure anatase TiO₂, which was brought on by nitrogen doping altering the local chemical environment of titanium ions. The successful doping of nitrogen into TiO₂@C, as shown by the test findings from XPS, has positive implications for reducing the band gap width of TiO₂ and increasing its visible light activity. We also tested the relative amount of C and N in the sample with an elemental analyzer. The content of nitrogen decreased with the increase in heat treatment temperature. A ratio as high as 0.12% N/C was obtained for the heat treatment of 450 °C.

The nitrogen adsorption–desorption isotherm samples for N-doped TiO₂@C-450 °C (Figure 2g) exhibited the conventional type IV isotherm and type H3 hysteresis loop. The pore size distribution was calculated using the nonlocal density function model (NLDFT) based on data from N₂ adsorption (Figure 2h). N-doped TiO₂@C-450 °C has a specific surface area of 63 m²/g, which is significantly less than that of NH₂-MIL-125 but still significantly larger than that of other TiO₂ catalysts. Therefore, basic fuchsin, rhodamine B and tetracycline hydrochloride can be degraded at more active sites thanks to the large specific surface area of N-doped TiO₂@C-450 °C.

BET data need to be interpreted in combination with thermogravimetric curves (Figure 2g,h, Table 1). The specific surface area of the samples decreased, and the average pore size increased with increasing roasting temperatures, but for different reasons. The sample changed at about 200 °C as a result of the elimination of any remaining solvent. When the temperature reached 350 °C, the porous structure collapsed, and the crystal skeleton began to disintegrate, greatly reducing the specific surface area. The decomposition of the crystal skeleton and the collapse of the porous structure made the specific surface area decrease sharply. When the calcination temperature was further increased to 450 °C, the BET data changed due to the recrystallization of TiO₂ and the formation of pyrolytic carbon substrates. However, the skeleton shrank significantly once more at 550 °C, and the specific surface area dropped to 13 m²/g, making it difficult for contaminants and the catalyst to make contact. Therefore, by adjusting the calcination temperature, the N-doped TiO₂@C catalyst with the best photocatalytic effect was created at 450 °C.

Table 1. Textural characteristics of NH₂-MIL-125, N-doped TiO₂@C-200 °C, N-doped TiO₂@C-350 °C, N-doped TiO₂@C-450 °C and N-doped TiO₂@C-550 °C.

Sample	S _{BET} (m ² g ⁻¹)	V _{total} (cm ³ g ⁻¹)	Average Pore Diameter (nm)	N/C *
NH ₂ -MIL-125	539	0.087	5.32	0.146
N-doped TiO ₂ @C-200 °C	763	0.168	6.54	0.0035
N-doped TiO ₂ @C-350 °C	89	0.157	9.30	0.0022
N-doped TiO ₂ @C-450 °C	63	0.141	10.89	0.0012
N-doped TiO ₂ @C-550 °C	13	0.046	12.26	0.0007

* The N/C value means atomic mass ratio, which was taken with a Eurovector EA 3000 elemental analyzer in CHN mode.

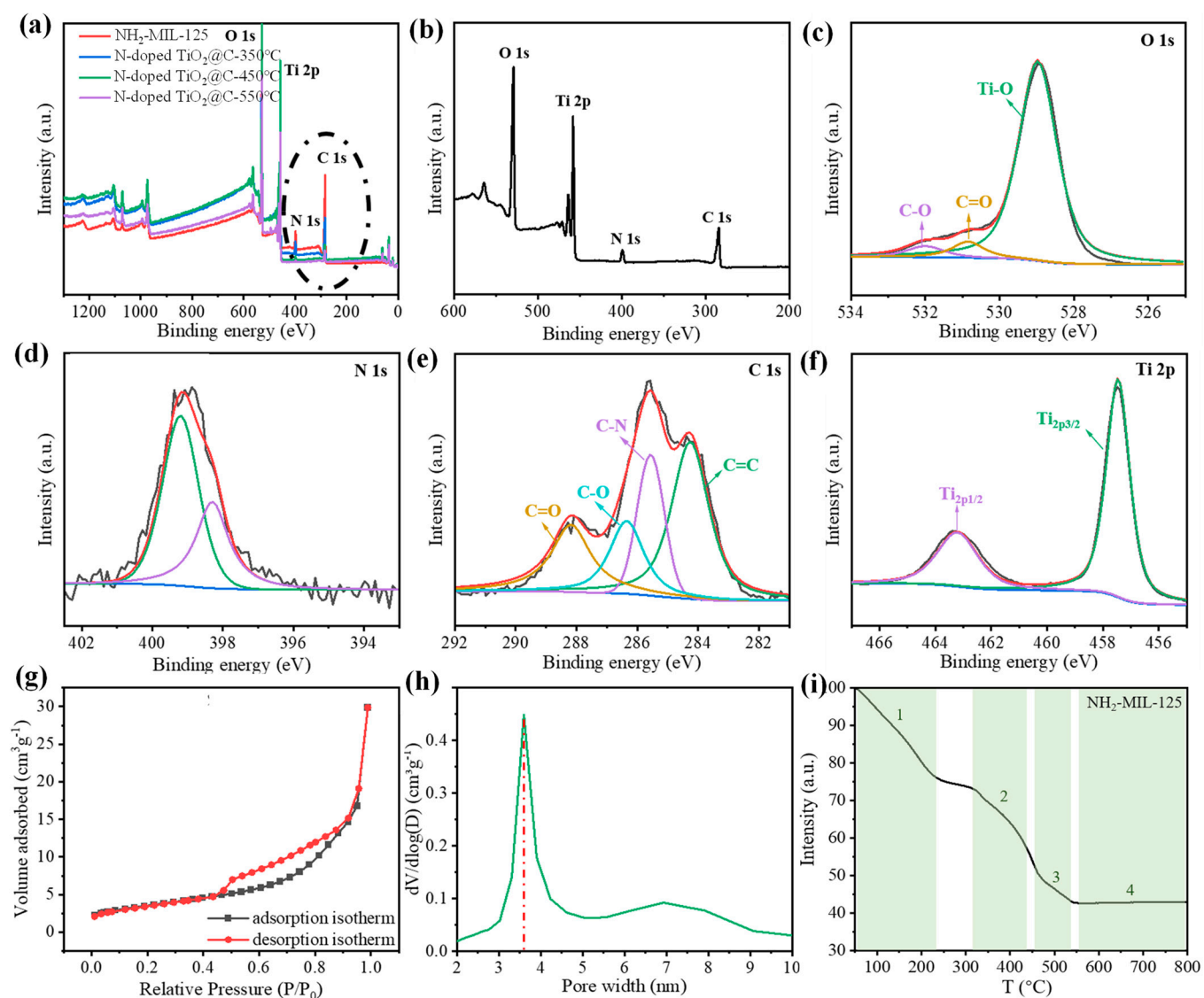


Figure 2. Chemical characterization of the N-doped $\text{TiO}_2@\text{C}$ composites. (a,b) Survey XPS spectra of $\text{NH}_2\text{-MIL-125}$, N-doped $\text{TiO}_2@\text{C-250}^\circ\text{C}$, N-doped $\text{TiO}_2@\text{C-350}^\circ\text{C}$, N-doped $\text{TiO}_2@\text{C-450}^\circ\text{C}$ and N-doped $\text{TiO}_2@\text{C-550}^\circ\text{C}$. High-resolution XPS spectra of (c) O 1s, (d) N 1s, (e) C 1s and (f) Ti 2p of N-doped $\text{TiO}_2@\text{C-450}^\circ\text{C}$. (g) N_2 adsorption–desorption isotherms of N-doped $\text{TiO}_2@\text{C-450}^\circ\text{C}$. (h) Pore size distributions of N-doped $\text{TiO}_2@\text{C-450}^\circ\text{C}$. (i) Thermogravimetric curve of $\text{NH}_2\text{-MIL-125}$.

3.2. Photocatalytic Degradation of N-Doped $\text{TiO}_2@\text{C}$

The light absorption capacity of N-doped $\text{TiO}_2@\text{C}$ composites was investigated via a UV–Vis absorption test (Figure 3a). $\text{NH}_2\text{-MIL-125}$ was yellow, as already described. The sample’s color continued to deepen as the calcination temperature rose due to the breakdown of the crystal skeleton and the collapse of the porous structure. The sample’s hue changed to brown at 350°C , when it exhibited the best ability to absorb visible light. As the calcination temperature increased after 350°C , TiO_2 crystals started to form, and the sample’s color lightened. The sample was nearly white at 550°C , and visible light could no longer be absorbed. We know that P25, the white commercial-grade TiO_2 , has poor absorption capabilities for visible light. The optimal catalyst for the best visible light absorption performance at 400–800 nm should be N-doped $\text{TiO}_2@\text{C-350}^\circ\text{C}$. However, the photocatalytic activity of N-doped $\text{TiO}_2@\text{C-350}^\circ\text{C}$ was subpar due to the absence of TiO_2 crystals. The most acceptable visible light catalyst, according to a thorough comparison

between the sample's photoabsorption capacity and TiO₂ content, was N-doped TiO₂@C-450 °C.

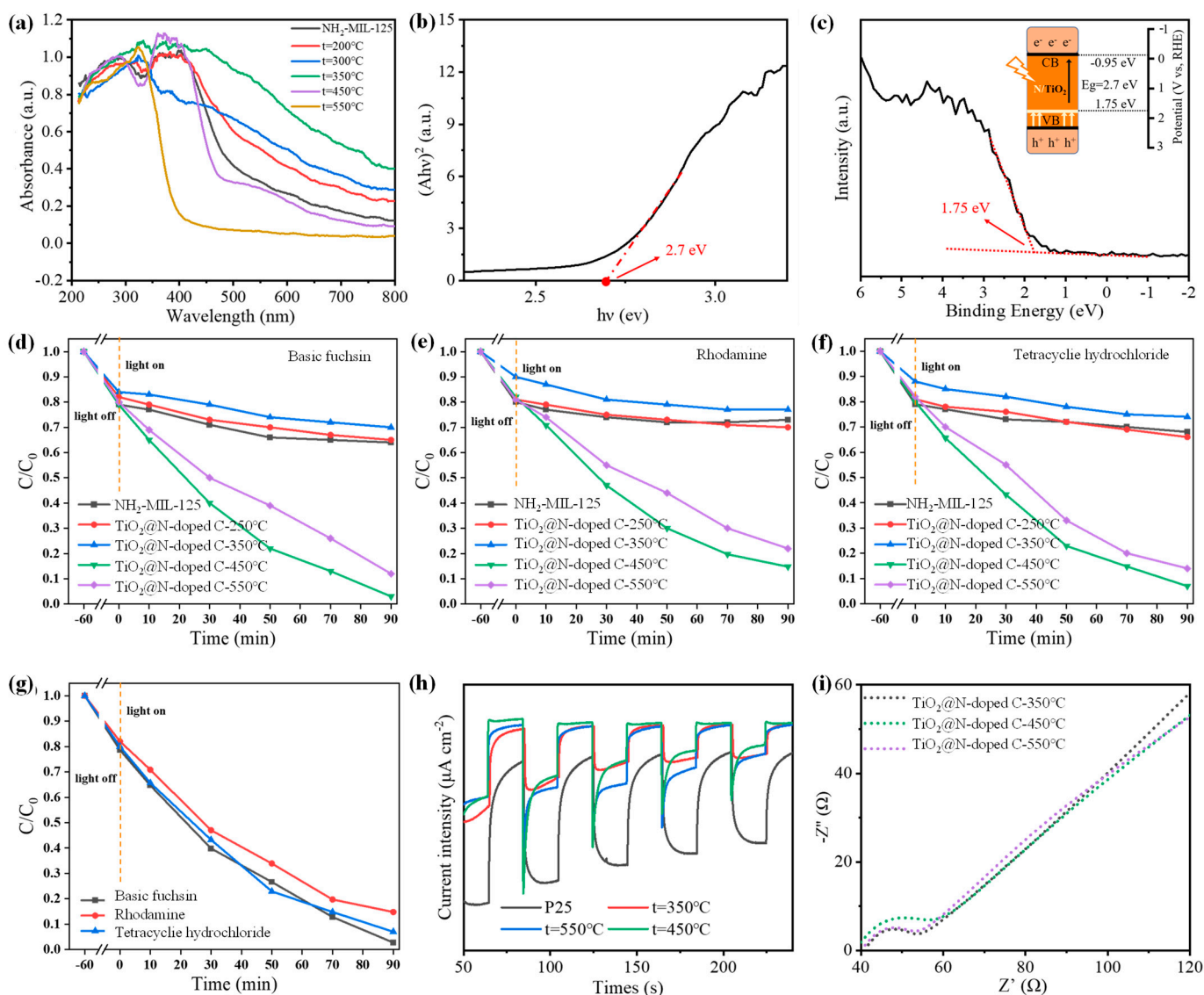


Figure 3. (a) DRS spectra for N-doped TiO₂@C with calcination temperatures of 200 °C, 300 °C, 350 °C, 450 °C and 550 °C and for NH₂-MIL-125. (b) Band gap and (c) valence band spectra of N-doped TiO₂@C-450 °C (with an energy level diagram of N-doped TiO₂@C-450 °C). Photocatalytic degradation efficiencies of (d) basic fuchsin, (e) Rhodamine B and (f) tetracycline hydrochloride over NH₂-MIL-125, N-doped TiO₂@C-200 °C, N-doped TiO₂@C-350 °C, N-doped TiO₂@C-450 °C and N-doped TiO₂@C-550 °C under xenon lamp irradiation. (g) Degradation plots of N-doped TiO₂@C-450 °C. (h) Transient photocurrent responses for N-doped TiO₂@C with calcination temperatures of 350 °C, 450 °C and 550 °C and for NH₂-MIL-125. (i) EIS Nyquist plots of N-doped TiO₂@C with calcination temperatures of 350 °C, 450 °C and 550 °C.

Compared with P25, the as-prepared N-doped TiO₂@C-450 °C sample had a wider absorption range, which was because nitrogen in the organic connector was released and doped into the sample during calcination, which reduced the wide band gap of TiO₂ and caused the light absorption range to shift to the visible region. The prohibited band spectra (Figure 3b) and valence band spectra (Figure 3c) of N-doped TiO₂@C-450 °C can be used to compute the energies of the valence band, conduction band and band gap, which were −0.95 eV, 1.75 eV and 2.7 eV, respectively. The N-doped TiO₂@C-450 °C band gap created in this work was narrower than that of anatase TiO₂, which had a band gap energy of 3.22 eV, making it more suitable for light absorption and photocatalytic processes.

Under xenon lamp illumination, the photocatalytic activity of N-doped TiO₂@C composites was assessed using dealcalized fuchsin, Rhodamine B and tetracycline hydrochloride. These three contaminants all degraded in a very similar way. Only NH₂-MIL-125 was capable of decomposing basic fuchsin (Figure 3d), lowering the pollutant concentration to 65%. This was because NH₂-MIL-125 can carry out a certain amount of physical adsorption due to its large specific surface area and micropore structure. The capability for deterioration varied significantly among N-doped TiO₂@C samples. At 350 °C, N-doped TiO₂@C exhibited the lowest degradation ability compared to other catalysts. N-doped TiO₂@C-350 °C showed the worst degradation ability, and 70% of basic fuchsin remained in the solution after degradation, even less than that of NH₂-MIL-125's adsorption effect. This was mainly due to two reasons. First, TiO₂ does not form at this temperature and prevents photocatalytic reactions; second, at 350 °C, NH₂-MIL-125 undergoes significant pyrolysis that rapidly changes its skeletal structure and reduces specific surface area sharply. Moreover, there was an overall increase in pore size, resulting in mesoporous pores and causing a decline in its adsorption effectiveness. Degradation of 99.7% of basic fuchsin with N-doped TiO₂@C-450 °C was the highest among all samples within 90 min. However, anatase TiO₂ obtained via the high-temperature heat treatment at 550 °C had the highest content and the best crystal form. However, the above characterization results indicate that the high-temperature heat treatment was not conducive to nitrogen doping and reduced the utilization efficiency of visible light. Consequently, the degradation efficiency of basic fuchsin was not as good as that achieved with N-doped TiO₂@C-450 °C.

The degradation of Rhodamine B and tetracycline hydrochloride exhibited similar trends in the above samples (Figure 3e,f). NH₂-MIL-125 achieved a 73% reduction in the content of Rhodamine B through physical adsorption. Among the tested catalysts, N-doped TiO₂@C-350 °C demonstrated the lowest degradation efficiency with only 23% of pollutants being degraded, whereas N-doped TiO₂@C-450 °C exhibited the highest degradation effect by degrading 89.9% of Rhodamine B within 90 min. Physical adsorption by NH₂-MIL-125 resulted in a decrease in the content of tetracycline hydrochloride to 68%. Similarly, N-doped TiO₂@C-350 °C showed inferior performance with only a 26% degradation rate for pollutants, whereas N-doped TiO₂@C-450 °C displayed superior degradation capability by achieving a remarkable removal rate of 93% for tetracycline hydrochloride within the same time frame (Figure 3g). In Table 2, we summarize the recent works on the degradation performance of TiO₂ composites against tetracycline. In comparison, our materials show outstanding catalytic properties [26].

Table 2. Summary of works on the degradation performance of TiO₂ composites against tetracycline.

Order	Catalyst	Light Source	Concentrations of Catalysts (g/L)	Concentrations of Pollutants (mg/L)	Degradation Efficiency	Time (h)	Reference
1	g-C ₃ N ₄ /TiO ₂	300 Xe (UV-Vis)	0.4	20	90.1%	1.0	[26]
2	TiO ₂ /Fe-MOF (15%)	300 Xe (UV-Vis, λ = 370 nm)	1	96	97%	4	[27]
3	TiO ₂ , H ₂ Ti ₃ O ₇	Xe lamp	0.02	20	89%, 94%	1	[28]
4	Biofilm-UCPs-TiO ₂	lamp (20 W) of 1800 Lux SPD-16 UV-vis detector at 357 nm	1	40	82.1%	24	[29]
5	Black-TiO ₂	200–800 nm by UV-Vis DRS	0.5	10	66.2%	4.5	[30]
6	AgBreTiO ₂ -Pal (50%)	300 Xe (λ > 400 nm)	0.5	10	89.6%	1.5	[31]
7	Defect-rich hydrogenated g-C ₃ N ₄ /TiO ₂	300 Xe (λ > 400 nm)	0.6	30	60%	1.5	[32]
8	N-TiO ₂ /Ov carbon nitride doped with oxygen	300 Xe (λ > 420 nm)	0.4	30	79.9%	1.0	[33]
9	Oxygen vacancies modified TiO ₂ /O-terminated Ti ₃ C ₂ composites	Vis (300 W)	0.4	20	88.5%	1.5	[34]
10	Ti ₃ C ₂ @TiO ₂	125 W Xe (λ > 400 nm)	1	20	90%	1.5	[35]
11	N-doped TiO ₂ @C	300 W Xe (λ > 420 nm)	0.67	30	93%	1.5	This work

Under xenon lamp irradiation, we used a photocurrent test to investigate the phenomenon of photogenerated carrier transport in samples. The photocurrent intensity of all N-doped TiO₂@C samples was relatively high, indicating a slow photogenerated carrier recombination rate (Figure 3h). This was mainly because TiO₂ was combined with the carbon matrix, and the porous structure of the carbon skeleton shortened the carrier transfer distance so that the photogenerated electron pairs could be effectively separated. In addition, the large specific surface area of the carbon skeleton exposed more active sites, making carrier transmission and diffusion more convenient. In short, the combination of carbon skeletons and TiO₂ enhanced the photocurrent intensity of the composite compared with commercial-grade TiO₂ P25. It is well known that the higher the photocurrent density, the better the ability to separate photogenerated electrons and holes. Therefore, compared with P25, N-doped TiO₂@C improves carrier separation efficiency and inhibits photogenerated carrier recombination. To confirm this, we further studied the resistance of interfacial charge conversion via electrochemical impedance spectroscopy. As shown in Figure 3i, the radii of all N-doped TiO₂@C composites were small, indicating that the N-doped TiO₂@C catalyst had higher interfacial charge separation efficiency and better electrical conductivity, which is similar to the trend in the photocurrent response test results. The charge transfer resistance (R_{ct}) of N-doped TiO₂@C in an equivalent circuit was smaller than that of pure TiO₂ [36], which further confirms the favored interfacial charge transfer.

In summary, the optimal balance between anatase TiO₂ formation and nitrogen doping was achieved when the calcination temperature reached 450 °C, and N-doped TiO₂@C-450 °C exhibited the highest photocatalytic capacity.

Tetracycline hydrochloride was used as an example to investigate the stability and reusability of the N-doped TiO₂@C-450 °C catalyst. The same sample was employed for five consecutive degradation cycles under identical conditions (Figure 4a). No significant

changes were observed after five cycles, although the degradation capacity decreased from 93% to 81%. This decrease in degradation capacity was primarily attributed to the blockage of mesoporous channels in N-doped $\text{TiO}_2\text{@C-450 }^\circ\text{C}$ by pollutants over prolonged reaction times, making it challenging to effectively clean and negatively impacting the recyclability of the catalyst. Additionally, the inevitable loss of the photocatalyst during repeated use also resulted in a decrease in degradation efficiency. Moreover, a comparison of SEM images, XRD spectra and XPS spectra (Figure 4b–d) before and after the reaction revealed that there was no significant change in the structure, morphology characteristics and chemical composition of N-doped $\text{TiO}_2\text{@C-450 }^\circ\text{C}$ before and after testing. N-doped $\text{TiO}_2\text{@C-450 }^\circ\text{C}$ exhibited excellent photocatalytic ability, stability and reusability; it has great potential as a visible photocatalyst for various types of pollutants.

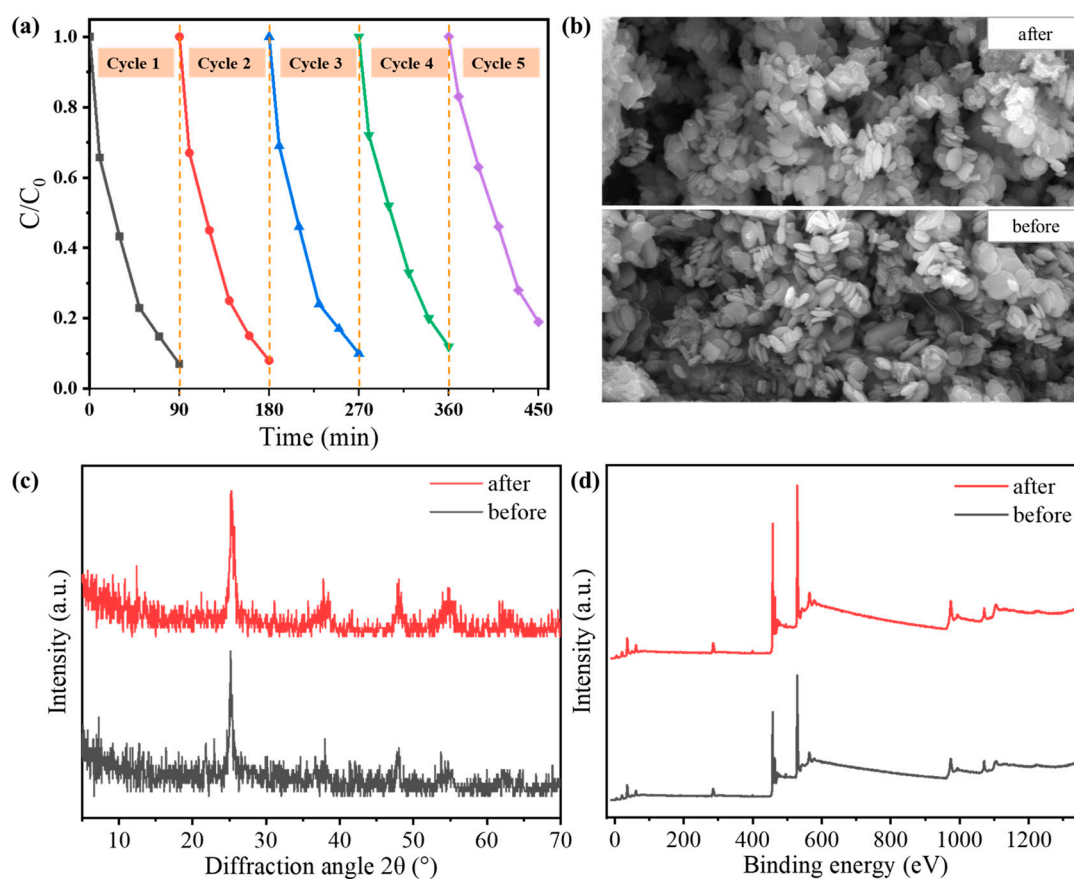


Figure 4. (a) Repeated experiments of tetracycline photodegradation over N-doped $\text{TiO}_2\text{@C-450 }^\circ\text{C}$. (b) SEM images, (c) XRD patterns and (d) XPS spectra of N-doped $\text{TiO}_2\text{@C-450 }^\circ\text{C}$ before and after the photocatalytic reaction.

3.3. Photocatalytic Mechanism

The photocatalytic mechanism of N-doped $\text{TiO}_2\text{@C-450 }^\circ\text{C}$ nanomaterials during visible light degradation was investigated by conducting multiple trapping experiments using tetracycline hydrochloride as an example. Three additional trapping reagents were added to the reaction solution, among which ammonium oxalate (AO) was used to trap e^- , benzoquinone (BQ) was used to trap $\text{O}_2^{\bullet-}$ and isopropyl alcohol (IPA) was used to trap OH^\bullet (Figure 5a). The addition of each trapping agent affected the degradation rate of tetracycline hydrochloride, among which isopropyl alcohol had the most prominent inhibitory effect among all trapping agents. The degradation efficiency of N-doped $\text{TiO}_2\text{@C-450 }^\circ\text{C}$ was reduced significantly to 71% after the addition of isopropyl alcohol, indicating that OH^\bullet plays a leading role in the degradation reaction of tetracycline hydrochloride under

visible light irradiation. In addition, the addition of ammonium oxalate and benzoquinone (BQ) also had a certain effect on the degradation rate, suggesting that e^- and $O_2^{\bullet-}$ were also involved in the process but did not play a major role. In conclusion, OH^\bullet was produced by the N-doped $TiO_2@C-450^\circ C$ catalyst during the photocatalysis process, which enhanced the oxidation capacity of the active substance and improved its ability to degrade tetracycline hydrochloride greatly.

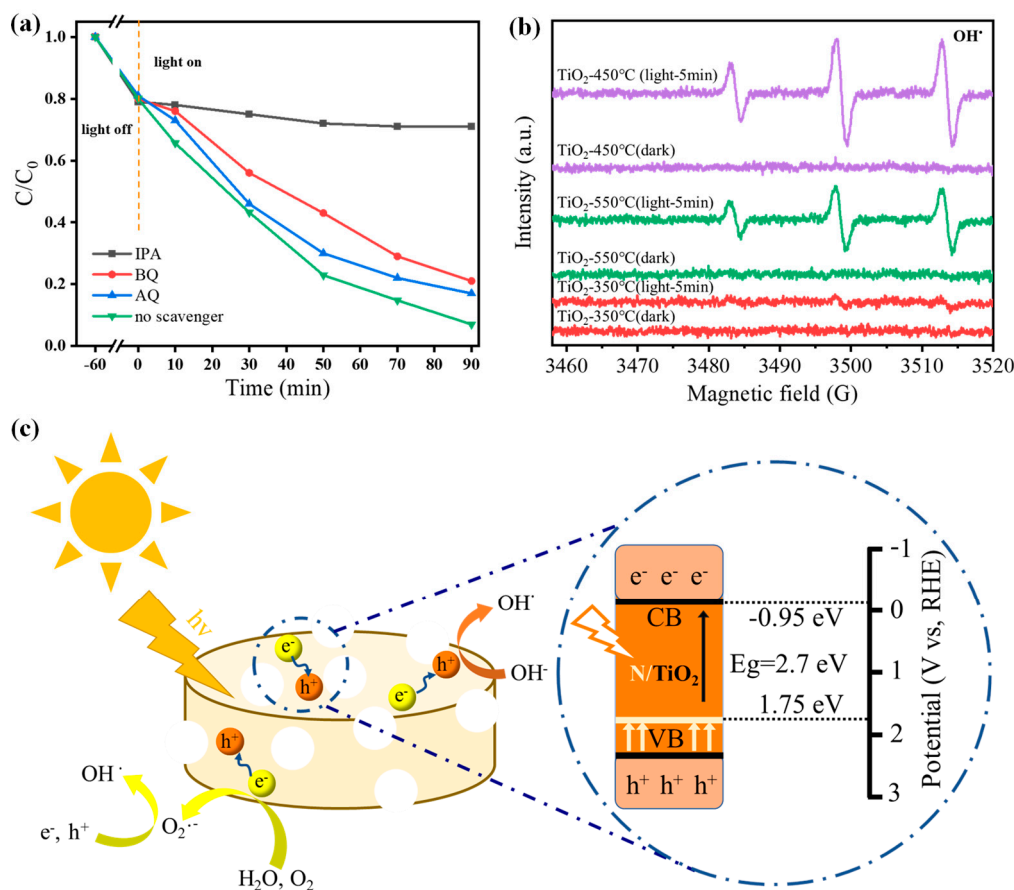


Figure 5. (a) Photocatalytic ability of N-doped $TiO_2@C-450^\circ C$ for the degradation of tetracycline with or without adding IPA, BQ and AQ under visible light. (b) EPR spectra of OH^\bullet on N-doped $TiO_2@C-350^\circ C$, N-doped $TiO_2@C-450^\circ C$ and N-doped $TiO_2@C-550^\circ C$ catalysts. (c) Probable photocatalytic mechanism of tetracycline degradation by N-doped $TiO_2@C-450^\circ C$ under visible light irradiation.

A DMPO trapping agent was added to the photocatalytic reaction system to detect active free radicals via EPR. Therefore, electron paramagnetic resonance spectroscopy was used to detect the signals of OH^\bullet radicals generated by N-doped $TiO_2@C-350^\circ C$, N-doped $TiO_2@C-450^\circ C$ and N-doped $TiO_2@C-550^\circ C$ under visible light irradiation (Figure 5b). Obviously, regardless of dark or light conditions, N-doped $TiO_2@C-350^\circ C$ OH^\bullet showed almost no occurrence of free radicals, and this was because the TiO_2 of N-doped $TiO_2@C-350^\circ C$ had not formed. For N-doped $TiO_2@C-450^\circ C$ and N-doped $TiO_2@C-550^\circ C$, almost no OH^\bullet free radicals increased. This indicates that the photogenerated electrons on anatase TiO_2 were transferred rapidly through the carbon skeleton, resulting in the production of a large number of OH^\bullet free radicals. N-doped $TiO_2@C-450^\circ C$ exhibited the highest number of OH^\bullet free radicals due to nitrogen doping, which enhanced the sample's utilization rate of visible light. This phenomenon further confirms the excellent photocatalytic effect of nitrogen-doped TiO_2 supported by a carbon skeleton, which can serve as photosensitizer to absorb visible light and help to promote charge carriers' separation through cooperation with bulk/surface defects of TiO_2 [37,38].

Based on the test results and analysis mentioned above, a possible photocatalytic reaction mechanism of N-doped TiO₂@C-450 °C can be proposed (Figure 5c). Under visible light irradiation, nitrogen-doped TiO₂ nanoparticles can efficiently produce charge carriers. At this stage, the unique porous structure of N-doped TiO₂@C-450 °C provides additional pathways for the movement of charge carriers, facilitating the easy transfer of electrons to the carbon framework and effectively separating photogenerated electrons and holes. During the degradation process, O₂•⁻ free radicals are generated through reactions between electrons enriched on the carbon framework with H₂O and O₂. It can be found that the REDOX potential of N-doped TiO₂@C CB positions is more negative than that of O₂/•O₂⁻, and the REDOX potential of VB positions is more positive than that of OH⁻/•OH, thus contributing to the generation of reactive oxygen species under photoexcitation [39,40].

4. Conclusions

In summary, we successfully synthesized a N-doped TiO₂@C composite material through NH₂-MIL-125 template-assisted calcination. Supported by the NH₂-MIL-125 carbon framework, the catalyst exhibited a significantly enhanced specific surface area of 63 m²/g, thereby facilitating an increased number of active sites for both the catalyst and reactant. The mesoporous structure (3.5 nm) of NH₂-MIL-125 facilitated enhanced light penetration, thereby reducing the occurrence of light shielding. Element mapping confirmed the presence of nitrogen, indicating that nitrogen was released from the organic ligand 2-amino-terephthalic acid and doped into the sample during calcination. Nitrogen doping in anatase shortened its wide band gap of 3.22 eV to 2.7 eV, resulting in a shift in the optical absorption range toward the visible region. As a result, the N-doped TiO₂@C catalyst exhibited extended optical absorption capabilities beyond just ultraviolet wavelengths. By carefully controlling the calcination temperature, we successfully synthesized various N-doped TiO₂@C composites. When calcined at 450 °C, the N-doped TiO₂@C catalyst achieved a balance between anatase content and nitrogen doping. The resulting N-doped TiO₂@C-450 °C composite exhibited outstanding performance in photocatalytic degradation. Under visible light for 90 min, basic fuchsin, Rhodamine B and tetracycline hydrochloride were degraded by 99.7%, 89.9% and 93% respectively. Moreover, the N-doped TiO₂@C-450 °C composite demonstrated excellent stability, as evidenced by negligible changes in SEM, XRD and XPS characteristics after five cycles of use; only a slight decrease in tetracycline hydrochloride degradation efficiency from 93% to 81% was observed. Last, we proposed the mechanism of photocatalytic degradation. This study presents a viable strategy for efficient pollution degradation under visible light.

Author Contributions: Conceptualization, C.C.; Methodology, W.W. and W.Q.; Validation, W.W. and W.Q.; Formal analysis, W.Q.; Investigation, W.W.; Resources, W.Q.; Data curation, W.W.; Writing—original draft preparation, W.W.; Writing—review and editing, C.C. and D.S.; Supervision, C.C. and D.S.; Funding acquisition, D.S. All authors have read and agreed to the published version of the manuscript.

Funding: This research was funded by the National Natural Science Foundation of China, grant numbers 51803092 and 51873087).

Institutional Review Board Statement: Not applicable.

Data Availability Statement: The data presented in this study are available on request from the corresponding author.

Conflicts of Interest: Author Wenbin Wang was employed by Guizhou Panjiang Civil Explosion Co., Ltd. The remaining authors declare that the research was conducted in the absence of any commercial or financial relationships that could be construed as potential conflicts of interest.

References

1. Hannah, D.M.; Abbott, B.W.; Khamis, K.; Kelleher, C.; Lynch, I.; Krause, S.; Ward, A.S. Illuminating the 'invisible water crisis' to address global water pollution challenges. *Hydrol. Process.* **2022**, *36*, e14525. [[CrossRef](#)]
2. Sehar, S.; Rasool, T.; Syed, H.M.; Mir, M.A.; Naz, I.; Rehman, A.; Shah, M.S.; Akhter, M.S.; Mahmood, Q.; Younis, A. Recent advances in biodecolorization and biodegradation of environmental threatening textile finishing dyes. *3 Biotech* **2022**, *12*, 186. [[CrossRef](#)] [[PubMed](#)]
3. Park, J.; Lee, T.H.; Kim, C.; Lee, S.A.; Choi, M.J.; Kim, H.; Yang, J.W.; Lim, J.; Jang, H.W. Hydrothermally obtained type-II heterojunction nanostructures of In₂S₃/TiO₂ for remarkably enhanced photoelectrochemical water splitting. *Appl. Catal. B Environ.* **2021**, *295*, 120276. [[CrossRef](#)]
4. Lu, Y.; Zang, Y.; Zhang, H.; Zhang, Y.; Wang, G.; Zhao, H. Meaningful comparison of photocatalytic properties of {001} and {101} faceted anatase TiO₂ nanocrystals. *Sci. Bull.* **2016**, *61*, 1003–1012. [[CrossRef](#)]
5. Tian, J.; Zhao, Z.; Kumar, A.; Boughton, R.I.; Liu, H. Recent progress in design, synthesis, and applications of one-dimensional TiO₂ nanostructured surface heterostructures: A review. *Chem. Soc. Rev.* **2014**, *43*, 6920–6937. [[CrossRef](#)]
6. Wang, J.; Wang, G.; Wang, X.; Wu, Y.; Su, Y.; Tang, H. 3D/2D direct Z-scheme heterojunctions of hierarchical TiO₂ microflowers/g-C₃N₄ nanosheets with enhanced charge carrier separation for photocatalytic H₂ evolution. *Carbon* **2019**, *149*, 618–626. [[CrossRef](#)]
7. Lin, L.; Yang, H.; Xu, X. Effects of water pollution on human health and disease heterogeneity: A review. *Surf. Interfaces* **2022**, *10*, 1088. [[CrossRef](#)]
8. Abdelhamid, H.N.; Sultan, S.; Mathew, A.P. Binder-free Three-dimensional (3D) printing of Cellulose-ZIF8 (CelloZIF-8) for water treatment and carbon dioxide (CO₂) adsorption. *Chem. Eng. J.* **2023**, *468*, 143567. [[CrossRef](#)]
9. Wang, Z.; Li, Y.; Cheng, Q.; Wang, X.; Wang, J.; Zhang, G. Sb-based photocatalysts for degradation of organic pollutants: A review. *J. Clean. Prod.* **2022**, *367*, 133060. [[CrossRef](#)]
10. Tobaldi, D.M.; Lajaunie, L.; Rozman, N.; Caetano, A.P.F.; Seabra, M.P.; Škapin, A.S.; Arenal, R.; Labrincha, J.A. Impact of the absolute rutile fraction on TiO₂ visible-light absorption and visible-light-promoted photocatalytic activity. *J. Photochem. Photobiol. A Chem.* **2019**, *382*, 111940. [[CrossRef](#)]
11. Sun, H.; Lu, W.; Zhao, J. Structure and reactivity of anatase TiO₂(001)-(1 × 4) surface. *J. Phys. Chem. C* **2018**, *122*, 14528–14536. [[CrossRef](#)]
12. Wei, C.; Lin, W.Y.; Zainal, Z.; Williams, N.E.; Zhu, K.; Kruzic, A.P.; Smith, R.L.; Rajeshwar, K. Bactericidal Activity of TiO₂ Photocatalyst in Aqueous Media: Toward a Solar-Assisted Water Disinfection System. *Environ. Sci. Technol.* **1994**, *28*, 934–938. [[CrossRef](#)] [[PubMed](#)]
13. Playford, H.Y. Variations in the local structure of nano-sized anatase TiO₂. *J. Solid State Chem.* **2020**, *288*, 121414. [[CrossRef](#)]
14. Kong, X.; Li, J.; Yang, C.; Tang, Q.; Wang, D. Fabrication of Fe₂O₃/g-C₃N₄@N-TiO₂ photocatalyst nanotube arrays that promote bisphenol A photodegradation under simulated sunlight irradiation. *Sep. Purif. Technol.* **2020**, *248*, 116924. [[CrossRef](#)]
15. Chen, L.; Zhou, X.; Jin, B.; Luo, J.; Xu, X.; Zhang, L.; Hong, Y. Heterojunctions in g-C₃N₄/B-TiO₂ nanosheets with exposed {001} plane and enhanced visible-light photocatalytic activities. *Int. J. Hydrogen Energy* **2016**, *41*, 7292–7300. [[CrossRef](#)]
16. Akbari, M.; Ghasemzadeh, M.A.; Fadaeian, M. Synthesis and application of ZIF-8 MOF incorporated in a TiO₂@Chitosan nanocomposite as a strong nanocarrier for the drug delivery of acyclovir. *ChemistrySelect* **2020**, *5*, 14564–14571. [[CrossRef](#)]
17. Yang, X.; Wang, Y.; Hu, Y.; Zhao, H.; Sun, Y.; Hua, K.; Chen, G. Interior supported hierarchical TiO₂@Co₃O₄ derived from MOF-on-MOF architecture with enhanced electrochemical properties for lithium storage. *ChemElectroChem* **2019**, *6*, 3657–3666. [[CrossRef](#)]
18. Chen, K.; Guo, H.-N.; Li, W.-Q.; Wang, Y.J. MOF-derived core-shell CoP@NC@TiO₂ composite as a high-performance anode material for Li-ion batteries. *Chem. Asian J.* **2021**, *16*, 322–328. [[CrossRef](#)]
19. Wang, Y.; Yu, W.; Geng, F.; Zhao, L.; Wang, Y. TiO₂@MOF photocatalyst for the synergetic oxidation of microcystin-LR and reduction of Cr(VI) in a media. *Catalysts* **2021**, *11*, 1186. [[CrossRef](#)]
20. He, X.; Fang, H.; Gosztola, D.J.; Jiang, Z.; Jena, P.; Wang, W.N. Mechanistic insight into photocatalytic pathways of MIL-100(Fe)/TiO₂ composites. *ACS Appl. Mater. Interfaces* **2019**, *11*, 12516–12524. [[CrossRef](#)]
21. Lee, D.T.; Zhao, J.; Oldham, C.J.; Peterson, G.W.; Parsons, G.N. UiO-66-NH₂ Metal–Organic Framework (MOF) nucleation on TiO₂, ZnO, and Al₂O₃ atomic layer deposition-treated polymer fibers: Role of metal oxide on MOF growth and catalytic hydrolysis of chemical warfare agent simulants. *ACS Appl. Mater. Interfaces* **2017**, *9*, 44847–44855. [[CrossRef](#)] [[PubMed](#)]
22. He, K.; Wen, Q.; Wang, C.; Wang, B.; Yu, S.; Hao, C.; Chen, K. Porous TiO₂ nanoparticles derived from titanium Metal–Organic Framework and its improved electrorheological performance. *Ind. Eng. Chem. Res.* **2018**, *57*, 6888–6896. [[CrossRef](#)]
23. Sheng, H.; Chen, D.; Li, N.; Xu, Q.; Li, H.; He, J.; Lu, J. Urchin-inspired TiO₂@MIL-101 double-shell hollow particles: Adsorption and highly efficient photocatalytic degradation of hydrogen sulfide. *Chem. Mater.* **2017**, *29*, 5612–5616. [[CrossRef](#)]
24. Zhou, S.; Guo, J.; Dai, Z.; Liu, C.; Zhao, J.; Gao, Z.; Song, Y.-Y. Engineering homochiral MOFs in TiO₂ nanotubes as enantioselective photoelectrochemical electrode for chiral recognition. *Anal. Chem.* **2021**, *93*, 12067–12074. [[CrossRef](#)] [[PubMed](#)]
25. Fu, N.; Ren, X.-C. Synthesis of double-shell hollow TiO₂@ZIF-8 nanoparticles with enhanced photocatalytic activities. *Front. Chem.* **2020**, *8*, 578847. [[CrossRef](#)] [[PubMed](#)]
26. Zhao, J.; Wang, B.; Zhao, Y.; Hou, M.; Xin, C.; Li, Q.; Yu, X. High-performance visible-light photocatalysis induced by dye-sensitized Ti³⁺-TiO₂ microspheres. *J. Phys. Chem. Solids* **2023**, *179*, 111374. [[CrossRef](#)]

27. Bi, R.; Liu, J.; Zhou, C.; Shen, Y.; Liu, Z.; Wang, Z. In situ synthesis of g-C₃N₄/TiO₂ heterojunction by a concentrated absorption process for efficient photocatalytic degradation of tetracycline hydrochloride. *Environ. Sci. Pollut. Res.* **2023**, *30*, 55044–55056. [[CrossRef](#)] [[PubMed](#)]
28. Feizpoor, S.; Habibi-Yangjeh, A.; Luque, R. Preparation of TiO₂/Fe-MOF n–n heterojunction photocatalysts for visible-light degradation of tetracycline hydrochloride. *Chemosphere* **2023**, *336*, 139101. [[CrossRef](#)]
29. Li, Y.; Liu, H.; Hou, C.; Xie, Y.; Wang, L.; Zhang, M. Transformation of titanium-based photocatalyst and its degradation of tetracycline hydrochloride. *J. Alloys Compd.* **2024**, *970*, 172644. [[CrossRef](#)]
30. Wang, Y.; Fan, H.; Wong, P.K.; Wu, Y.; Rittmann, B. Biodegradation of tetracycline using hybrid material (UCPs-TiO₂) coupled with biofilms under visible light. *Bioresour. Technol.* **2021**, *323*, 124638. [[CrossRef](#)]
31. Wu, S.; Li, X.; Tian, Y.; Lin, Y.; Hu, Y.H. Excellent photocatalytic degradation of tetracycline over black anatase-TiO₂ under visible light. *Chem. Eng. J.* **2021**, *406*, 126747. [[CrossRef](#)]
32. Shi, Y.; Yan, Z.; Xu, Y.; Tian, T.; Zhang, J.; Pang, J.; Peng, X.; Zhang, Q.; Shao, M.; Tan, W.; et al. Visible-light-driven AgBr/TiO₂-Palygorskite photocatalyst with excellent photocatalytic activity for tetracycline hydrochloride. *J. Clean. Prod.* **2020**, *277*, 124021. [[CrossRef](#)]
33. Ning, P.; Chen, H.; Pan, J.; Liang, J.; Qin, L.; Chen, D.; Huang, Y. Surface defect-rich g-C₃N₄/TiO₂ Z-scheme heterojunction for efficient photocatalytic antibiotic removal: Rational regulation of free radicals and photocatalytic mechanism. *Catal. Sci. Technol.* **2020**, *10*, 8295–8304. [[CrossRef](#)]
34. Wang, Y.; Lei, R.B.; Pw, A.; Zs, A.; Lz, A. Photocatalytic activity of N-TiO₂/O-doped N vacancy g-C₃N₄ and the intermediates toxicity evaluation under tetracycline hydrochloride and Cr(VI) coexistence environment. *Appl. Catal. B Environ.* **2020**, *262*, 118308. [[CrossRef](#)]
35. Zhou, S.; Jiang, L.; Wang, H.; Yang, J.; Yuan, X.; Wang, H.; Liang, J.; Li, X.; Li, H.; Bu, Y. Oxygen Vacancies Modified TiO₂/O-Terminated Ti₃C₂ Composites: Unravelling the Dual Effects between Oxygen Vacancy and High-Work-Function Titanium Carbide. *Adv. Funct. Mater.* **2023**, *33*, 2307702. [[CrossRef](#)]
36. Biswal, L.; Mishra, B.P.; Das, S.; Acharya, L.; Nayak, S.; Parida, K. Nanoarchitecture of a Ti₃C₂@TiO₂ Hybrid for Photocatalytic Antibiotic Degradation and Hydrogen Evolution: Stability, Kinetics, and Mechanistic Insights. *Inorg. Chem.* **2023**, *62*, 7584–7597. [[CrossRef](#)] [[PubMed](#)]
37. Qu, X.; Lin, J.; Qiang, W.; Chen, C.; Sun, D. Self-doped defect-mediated TiO₂ with disordered surface for high-efficiency photodegradation of various pollutants. *Chemosphere* **2022**, *308*, 136239. [[CrossRef](#)] [[PubMed](#)]
38. Liu, J.; Han, L.; An, N.; Xing, L.; Ma, H.; Cheng, L.; Yang, J.; Zhang, Q. Enhanced visible-light photocatalytic activity of carbonate-doped anatase TiO₂ based on the electron-withdrawing bidentate carboxylate linkage. *Appl. Catal. B Environ.* **2017**, *202*, 642–652. [[CrossRef](#)]
39. Imparato, C.; Iervolino, G.; Fantauzzi, M.; Koral, C.; Macyk, W.; Kobielski, M.; D’Errico, G.; Rea, I.; Di Girolamo, R.; De Stefano, L.; et al. Photocatalytic hydrogen evolution by co-catalyst-free TiO₂/C bulk heterostructures synthesized under mild conditions. *RSC Adv.* **2020**, *10*, 12519–12534. [[CrossRef](#)]
40. Pukdeejorhor, L.; Wannapaiboon, S.; Berger, J.; Rodewald, K.; Thongratkaew, S.; Impeng, S.; Warnan, J.; Bureekaew, S.; Fischer, R.A. Defect engineering in MIL-125-(Ti)-NH₂ for enhanced photocatalytic H₂ generation. *J. Mater. Chem. A* **2023**, *11*, 9143–9151. [[CrossRef](#)]

Disclaimer/Publisher’s Note: The statements, opinions and data contained in all publications are solely those of the individual author(s) and contributor(s) and not of MDPI and/or the editor(s). MDPI and/or the editor(s) disclaim responsibility for any injury to people or property resulting from any ideas, methods, instructions or products referred to in the content.